

# Characterization of semiconductor materials using synchrotron radiation-based near-field infrared microscopy and nano-FTIR spectroscopy

Peter Hermann,<sup>1,\*</sup> Arne Hoehl,<sup>1</sup> Georg Ulrich,<sup>2</sup> Claudia Fleischmann,<sup>3</sup> Antje Hermelink,<sup>4</sup> Bernd Kästner,<sup>1</sup> Piotr Patoka,<sup>2</sup> Andrea Hornemann,<sup>1</sup> Burkhard Beckhoff,<sup>1</sup> Eckart Rühl,<sup>2</sup> and Gerhard Ulm<sup>1</sup>

<sup>1</sup>Physikalisch-Technische Bundesanstalt (PTB), Abbestraße 2-12, 10587 Berlin, Germany

<sup>2</sup>Physikalische und Theoretische Chemie, Institut für Chemie und Biochemie, Freie Universität Berlin, Takustraße 3, 14195 Berlin, Germany

<sup>3</sup>Imec, Kapeldreef 75, 3001 Leuven, Belgium

<sup>4</sup>Robert Koch-Institut, Seestraße 10, 13353 Berlin, Germany

\*[peter.hermann@ptb.de](mailto:peter.hermann@ptb.de)

**Abstract:** We describe the application of scattering-type near-field optical microscopy to characterize various semiconducting materials using the electron storage ring Metrology Light Source (MLS) as a broadband synchrotron radiation source. For verifying high-resolution imaging and nano-FTIR spectroscopy we performed scans across nanoscale Si-based surface structures. The obtained results demonstrate that a spatial resolution below 40 nm can be achieved, despite the use of a radiation source with an extremely broad emission spectrum. This approach allows not only for the collection of optical information but also enables the acquisition of near-field spectral data in the mid-infrared range. The high sensitivity for spectroscopic material discrimination using synchrotron radiation is presented by recording near-field spectra from thin films composed of different materials used in semiconductor technology, such as SiO<sub>2</sub>, SiC, Si<sub>x</sub>N<sub>y</sub>, and TiO<sub>2</sub>.

©2014 Optical Society of America

**OCIS codes:** (120.0120) Instrumentation, measurement, and metrology; (180.4243) Near-field microscopy; (240.0240) Optics at surfaces; (300.0300) Spectroscopy; (310.6860) Thin films, optical properties.

---

## References and links

1. M. Born and E. Wolf, *Principles of Optics: Electromagnetic Theory of Propagation, Interference and Diffraction of Light* (Cambridge University, 2002).
2. L. Novotny and B. Hecht, *Principles of Nano-Optics*, 2nd ed. (Cambridge University, 2012).
3. A. Zayats and D. Richards, eds., *Nano-Optics and Near-Field Optical Microscopy* (Artech House, 2009).
4. N. Mauser and A. Hartschuh, "Tip-enhanced near-field optical microscopy," *Chem. Soc. Rev.* **43**(4), 1248–1262 (2014).
5. S. Kawata and Y. Inouye, "Scanning probe optical microscopy using a metallic probe tip," *Ultramicroscopy* **57**(2–3), 313–317 (1995).
6. F. Zenhausern, Y. Martin, and H. K. Wickramasinghe, "Scanning interferometric apertureless microscopy: Optical imaging at 10 angstrom resolution," *Science* **269**(5227), 1083–1085 (1995).
7. R. Bachelot, P. Gleyzes, and A. C. Boccarda, "Near-field optical microscope based on local perturbation of a diffraction spot," *Opt. Lett.* **20**(18), 1924–1926 (1995).
8. B. Knoll and F. Keilmann, "Near-field probing of vibrational absorption for chemical microscopy," *Nature* **399**(6732), 134–137 (1999).
9. R. Hillenbrand, and F. Keilmann, "Complex optical constants on a subwavelength scale," *Phys. Rev. Lett.* **85**, 3029–3032 (2000).
10. M. B. Raschke and C. Lienau, "Apertureless near-field optical microscopy: Tip-sample coupling in elastic light scattering," *Appl. Phys. Lett.* **83**(24), 5089–5091 (2003).

11. A. Bek, R. Vogelgesang, and K. Kern, "Apertureless scanning near-field optical microscope with sub-10 nm resolution," *Rev. Sci. Instrum.* **77**(4), 043703 (2006).
12. M. Böhmler, Z. Wang, A. Myalitsin, A. Mews, and A. Hartschuh, "Optical imaging of CdSe nanowires with nanoscale resolution," *Angew. Chem. Int. Ed. Engl.* **50**(48), 11536–11538 (2011).
13. M. Paulite, C. Blum, T. Schmid, L. Opilik, K. Eyer, G. C. Walker, and R. Zenobi, "Full spectroscopic tip-enhanced Raman imaging of single nanotapes formed from B-amyloid(1-40) peptide fragments," *ACS Nano* **7**(2), 911–920 (2013).
14. P. Hermann, M. Hecker, D. Chumakov, M. Weisheit, J. Rinderknecht, A. Shelaev, P. Dorozhkin, and L. M. Eng, "Imaging and strain analysis of nano-scale SiGe structures by tip-enhanced Raman spectroscopy," *Ultramicroscopy* **111**(11), 1630–1635 (2011).
15. P. Hermann, H. Fabian, D. Naumann, and A. Hermelink, "Comparative study of far-field and near-field Raman spectra from silicon-based samples and biological nanostructures," *J. Phys. Chem. C* **115**(50), 24512–24520 (2011).
16. M. B. Raschke, L. Molina, T. Elsaesser, D. H. Kim, W. Knoll, and K. Hinrichs, "Apertureless near-field vibrational imaging of block-copolymer nanostructures with ultrahigh spatial resolution," *ChemPhysChem* **6**(10), 2197–2203 (2005).
17. S. Amarie, T. Ganz, and F. Keilmann, "Mid-infrared near-field spectroscopy," *Opt. Express* **17**(24), 21794–21801 (2009).
18. T. Taubner, F. Keilmann, and R. Hillenbrand, "Nanoscale-resolved subsurface imaging by scattering-type near-field optical microscopy," *Opt. Express* **13**(22), 8893–8899 (2005).
19. M. L. Daus, K. Wagenführ, A. Thomzig, S. Boerner, P. Hermann, A. Hermelink, M. Beekes, and P. Lasch, "Infrared microspectroscopy detects protein misfolding cyclic amplification (PMCA)-induced conformational alterations in hamster scrapie Progeny seeds," *J. Biol. Chem.* **288**(49), 35068–35080 (2013).
20. A. J. Huber, D. Kazantsev, F. Keilmann, J. Wittborn, and R. Hillenbrand, "Simultaneous IR material recognition and conductivity mapping by nanoscale near-field microscopy," *Adv. Mater.* **19**(17), 2209–2212 (2007).
21. U. Schade, K. Hollmack, P. Kuske, G. Wüstefeld, and H.-W. Hübers, "THz near-field imaging employing synchrotron radiation," *Appl. Phys. Lett.* **84**(8), 1422–1424 (2004).
22. K. Wang, D. M. Mittleman, N. C. J. van der Valk, and P. C. M. Planken, "Antenna effects in terahertz apertureless near-field optical microscopy," *Appl. Phys. Lett.* **85**(14), 2715–2717 (2004).
23. F. Bueersgens, R. Kersting, and H.-T. Chen, "Terahertz microscopy of charge carriers in semiconductors," *Appl. Phys. Lett.* **88**(11), 112115 (2006).
24. H.-G. von Ribbeck, M. Brehm, D. W. van der Weide, S. Winnerl, O. Drachenko, M. Helm, and F. Keilmann, "Spectroscopic THz near-field microscopy," *Opt. Express* **16**(5), 3430–3438 (2008).
25. S. C. Kehr, M. Cebula, O. Mieth, T. Härtling, J. Seidel, S. Grafström, L. M. Eng, S. Winnerl, D. Stehr, and M. Helm, "Anisotropy contrast in phonon-enhanced apertureless near-field microscopy using a free-electron laser," *Phys. Rev. Lett.* **100**(25), 256403 (2008).
26. K. Moon, E. Jung, M. Lim, Y. Do, and H. Han, "Terahertz near-field microscope: Analysis and measurement of scattering signals," *IEEE Trans. THz Sci. Technol.* **1**, 164–168 (2011).
27. A. J. Huber, J. Wittborn, and R. Hillenbrand, "Infrared spectroscopic near-field mapping of single nanotransistors," *Nanotechnology* **21**(23), 235702 (2010).
28. J. M. Stiegler, A. J. Huber, S. L. Diedenhofen, J. Gómez Rivas, R. E. Algra, E. P. A. M. Bakkers, and R. Hillenbrand, "Nanoscale free-carrier profiling of individual semiconductor nanowires by infrared near-field nanoscopy," *Nano Lett.* **10**(4), 1387–1392 (2010).
29. J. M. Hoffmann, B. Hauer, and T. Taubner, "Antenna-enhanced infrared near-field nanospectroscopy of a polymer," *Appl. Phys. Lett.* **101**(19), 193105 (2012).
30. F. Huth, A. Govyadinov, S. Amarie, W. Nuansing, F. Keilmann, and R. Hillenbrand, "Nano-FTIR absorption spectroscopy of molecular fingerprints at 20 nm spatial resolution," *Nano Lett.* **12**(8), 3973–3978 (2012).
31. B. Pollard, E. A. Muller, K. Hinrichs, and M. B. Raschke, "Vibrational nano-spectroscopic imaging correlating structure with intermolecular coupling and dynamics," *Nat. Commun.* **5**, 3587 (2014).
32. I. Amenabar, S. Poly, W. Nuansing, E. H. Hubrich, A. A. Govyadinov, F. Huth, R. Krutokhvostov, L. Zhang, M. Knez, J. Heberle, A. M. Bittner, and R. Hillenbrand, "Structural analysis and mapping of individual protein complexes by infrared nanospectroscopy," *Nat. Commun.* **4**, 2890 (2013).
33. M. Paulite, Z. Fakhraai, I. T. S. Li, N. Gunari, A. E. Tanur, and G. C. Walker, "Imaging secondary structure of individual amyloid fibrils of a  $\beta_2$ -microglobulin fragment using near-field infrared spectroscopy," *J. Am. Chem. Soc.* **133**(19), 7376–7383 (2011).
34. A. M. Gigler, A. J. Huber, M. Bauer, A. Ziegler, R. Hillenbrand, and R. W. Stark, "Nanoscale residual stress-field mapping around nanoindentations in SiC by IR s-SNOM and confocal Raman microscopy," *Opt. Express* **17**(25), 22351–22357 (2009).
35. Z. Fei, G. O. Andreev, W. Bao, L. M. Zhang, A. S. McLeod, C. Wang, M. K. Stewart, Z. Zhao, G. Dominguez, M. Thiemens, M. M. Fogler, M. J. Tauber, A. H. Castro-Neto, C. N. Lau, F. Keilmann, and D. N. Basov, "Infrared nanoscopy of Dirac plasmons at the graphene-SiO<sub>2</sub> interface," *Nano Lett.* **11**(11), 4701–4705 (2011).
36. J. Chen, M. Badioli, P. Alonso-González, S. Thongrattanasiri, F. Huth, J. Osmond, M. Spasenović, A. Centeno, A. Pesquera, P. Godignon, A. Z. Elorza, N. Camara, F. J. García de Abajo, R. Hillenbrand, and F. H. L. Koppens, "Optical nano-imaging of gate-tunable graphene plasmons," *Nature* **487**(7405), 77–81 (2012).

37. M. Ishikawa, M. Katsura, S. Nakashima, K. Aizawa, T. Inoue, H. Okamura, and Y. Ikemoto, "Modulated near-field spectral extraction of broadband mid-infrared signals with a ceramic light source," *Opt. Express* **19**(13), 12469–12479 (2011).
38. F. Huth, M. Schnell, J. Wittborn, N. Ocelic, and R. Hillenbrand, "Infrared-spectroscopic nanoimaging with a thermal source," *Nat. Mater.* **10**(5), 352–356 (2011).
39. I. M. Craig, M. S. Taubman, A. S. Lea, M. C. Phillips, E. E. Josberger, and M. B. Raschke, "Infrared near-field spectroscopy of trace explosives using an external cavity quantum cascade laser," *Opt. Express* **21**(25), 30401–30414 (2013).
40. Y. Ikemoto, T. Moriwaki, T. Kinoshita, M. Ishikawa, S. Nakashima, and H. Okamura, "Near-field spectroscopy with infrared synchrotron radiation source," *e-J. Surf. Sci. Nanotech.* **9**, 63–66 (2011).
41. D. A. Schmidt, E. Bründermann, and M. Havenith, "Combined far- and near-field chemical nanoscope at ANKA-IR2: applications and detection schemes," *J. Phys. Conf. Ser.* **359**, 012015 (2012).
42. P. Hermann, A. Hoehl, P. Patoka, F. Huth, E. Rühl, and G. Ulm, "Near-field imaging and nano-Fourier-transform infrared spectroscopy using broadband synchrotron radiation," *Opt. Express* **21**(3), 2913–2919 (2013).
43. H. A. Bechtel, E. A. Muller, R. L. Olmon, M. C. Martin, and M. B. Raschke, "Ultrabroadband infrared nanospectroscopic imaging," *Proc. Natl. Acad. Sci.*, published ahead of print (2014).
44. J. Feikes, M. von Hartrott, M. Ries, P. Schmid, G. Wüstefeld, A. Hoehl, R. Klein, R. Müller, and G. Ulm, "Metrology Light Source: The first electron storage ring optimized for generating coherent THz radiation," *Phys. Rev. ST Accel. Beams* **14**(3), 030705 (2011).
45. R. Müller, A. Hoehl, A. Matschulat, A. Serdyukov, G. Ulm, J. Feikes, M. Ries, and G. Wüstefeld, "Status of the IR and THz beamlines at the metrology light source," *J. Phys. Conf. Ser.* **359**, 012004 (2012).
46. R. Hillenbrand, T. Taubner, and F. Keilmann, "Phonon-enhanced light matter interaction at the nanometre scale," *Nature* **418**(6894), 159–162 (2002).
47. A. J. Huber, A. Ziegler, T. Köck, and R. Hillenbrand, "Infrared nanoscopy of strained semiconductors," *Nat. Nanotechnol.* **4**(3), 153–157 (2009).
48. S. Amarie and F. Keilmann, "Broadband-infrared assessment of phonon resonance in scattering-type near-field microscopy," *Phys. Rev. B* **83**(4), 045404 (2011).
49. M. Ishikawa, M. Katsura, S. Nakashima, Y. Ikemoto, and H. Okamura, "Broadband near-field mid-infrared spectroscopy and application to phonon resonances in quartz," *Opt. Express* **20**(10), 11064–11072 (2012).
50. L. M. Zhang, G. O. Andreev, Z. Fei, A. S. McLeod, G. Dominguez, M. Thiemens, A. H. Castro-Neto, D. N. Basov, and M. M. Fogler, "Near-field spectroscopy of silicon dioxide thin films," *Phys. Rev. B* **85**(7), 075419 (2012).
51. C. Pecharromán, F. Gracia, J. P. Holgado, M. Ocana, A. R. Gonzalez-Elipse, J. Bassas, J. Santiso, and A. Figueras, "Determination of texture by infrared spectroscopy in titanium oxide-apatite thin films," *J. Appl. Phys.* **93**(8), 4634–4645 (2003).
52. E. F. Krimmel, E. F. Hockings, and D. Schiöberg, *Gmelin Handbook of Inorganic and Organometallic Chemistry. – System Number 15: Si. Silicon. – Supplement Volume B5b2: Silicon Nitride: Electronic Structure, Electrical, Magnetic, and Optical Properties: Spectra: Analysis* (Springer, 1997).
53. M. Sunkara, S. Sharma, H. Chandrasekaran, M. Talbott, K. Krogman, and G. Bhimarasetti, "Bulk synthesis of a-Si<sub>3</sub>N<sub>4</sub>H and a-Si<sub>3</sub>O, straight and coiled nanowires," *J. Mater. Chem.* **14**(4), 590–594 (2004).
54. G. Scardera, T. Puzzer, G. Conibeer, and M. A. Green, "Fourier transform infrared spectroscopy of annealed silicon-rich nitride thin films," *J. Appl. Phys.* **104**(10), 104310 (2008).
55. S. C. Jain, H. E. Maes, K. Pinaridi, and I. De Wolf, "Stresses and strains in lattice-mismatched stripes, quantum wires, quantum dots, and substrates in Si technology," *J. Appl. Phys.* **79**(11), 8145–8165 (1996).
56. P. Hermann, M. Hecker, F. Renn, M. Rölke, K. Kolanek, J. Rinderknecht, and L. M. Eng, "Effects of patterning induced stress relaxation in strained SOI/SiGe layers and substrate," *J. Appl. Phys.* **109**(12), 124513 (2011).

## 1. Introduction

Photons with an energy in the range between terahertz (THz) to ultraviolet can induce a large number of light-matter interactions which can be exploited to gain information about various sample properties. Therefore, spectroscopic methods are nowadays widely used in different fields of physics, material science, chemistry, biology, and medicine. The achievable spatial resolution of these optical techniques is, however, limited by diffraction [1] to about half of the wavelength. This prevents to reach a lateral resolution below a few hundred nm when utilizing photons in the visible range, several microns in the mid-infrared (IR) range, and a few hundred microns in the THz range. This limitation can be circumvented by applying near-field based techniques [2–4], such as scattering-type near-field optical microscopy (s-SNOM) [5–8]. This method, often based on the principle of an atomic force microscope (AFM), utilizes a sharp metal-coated or solid metal tip which is brought into close proximity to the sample surface. Subsequent raster scanning of the sample provides both topographic data and information about the optical properties of the surface with a significantly improved lateral

resolution when compared to conventional far-field techniques. For this purpose the near-field probe is irradiated by a focused photon beam. Under optimized conditions the illuminated tip acts as an antenna that confines the incident electric field around the tip-apex, thus providing a nanoscale light source for high-resolution imaging. Depending on the wavelength of the incident photons and by analyzing the scattered light with a spectrometer system, sample properties in the visible [9–15], IR [16–20], and THz [21–26] regime can be investigated with the additional benefit of a significantly improved spatial resolution. For wavelengths in the IR regime this technique has already been applied to many different sample systems, e.g. for mapping of free carriers in transistors [27], determination of doping profiles in semiconductor structures and nanowires [28], mapping of the composition of polymers [29–31] and biological samples [32, 33], measurement of strain fields due to small spectral bandshifts [34], and the excitation of plasmons in metal nanostructures and graphene layers [35, 36]. For IR spectroscopic characterization of samples with unknown material composition it is desirable to have radiation sources capable of covering a large frequency range in the mid-IR regime. Various radiation sources have been evaluated during the last years for near-field IR spectroscopy. This includes tunable gas lasers with a rather limited accessible spectral range, thermal sources [37, 38], quantum cascade lasers [39], and synchrotron radiation [40, 41]. Successful nano-FTIR measurements using synchrotron radiation were recently demonstrated on partially Au-coated SiC samples [42]. Yet, for a better evaluation of the capability of this approach additional experiments are required involving more challenging samples are required, which is subject of the present study. A recent study demonstrated the capability of this approach for characterizing biological samples [43].

In the present work, we report on high-resolution imaging and nano-FTIR spectroscopy using the electron storage ring Metrology Light Source (MLS) [44] as an ultra-broadband synchrotron radiation source. In order to demonstrate that the achievable lateral resolution is comparable to the results reported for laser sources, we performed near-field measurements on patterned semiconductor samples. Compared to conventional thermal sources, such as a globar, an electron storage ring provides a broad emission spectrum from the near- to the far-IR as well as radiation with a defined polarization and higher brilliance as is advantageous for IR spectroscopy. The high sensitivity of this technique and its material discrimination capability are demonstrated by the acquisition of nano-FTIR spectra from materials relevant in semiconductor technology such as SiC, SiO<sub>2</sub>, TiO<sub>2</sub> and Si<sub>x</sub>N<sub>y</sub>.

## 2. Experimental part

The experiments described in the following were performed on a commercially available scattering-type scanning near-field optical microscope (Neaspec GmbH, Germany) consisting of an AFM and an asymmetric Michelson interferometer. The AFM was operated in tapping mode with a typical oscillation amplitude of about 50 nm. For the experiments Au-coated silicon-based AFM cantilevers with a resonance frequency between 76 and 263 kHz were used. The Au-coated tips had a diameter below 50 nm.

The MLS is a low-energy storage ring (629 MeV electron energy) which is especially designed for generating brilliant far-IR and THz radiation [44]. In standard operation mode the MLS (ring circumference 48 m) is operated with 80 electron bunches providing a pulse repetition rate of 500 MHz with a bunch length of about 25 ps. The IR radiation is coupled out from the ring at a bending magnet by a planar water cooled mirror and guided to the experimental setup by several planar and cylindrical mirrors [45]. At the end of the beamline, where a diamond window separates the ultra-high vacuum from the ambient condition under which the s-SNOM is operated, the rectangular-shaped IR beam has the dimensions of approximately 25 mm (horizontal) and 10 mm (vertical). The measured power at a ring current of 100 mA in the wavelength range from 1 μm to 20 μm is about 1.95 mW. In order to match the aperture of the instrumental optics the beam size can be reduced to approximately 10 mm (horizontal) and 10 mm (vertical) by using an arrangement of two parabolic mirrors. A

second periscope-like mirror arrangement converts the horizontal polarization of the synchrotron radiation into vertical polarization. The latter is more advantageous for s-SNOM experiments, since the electric field vector has a larger component parallel to the tip-axis thus increasing the electric field enhancement at the tip apex. The backscattered radiation from the sample is analyzed by a Michelson interferometer consisting of a reference arm with a planar mirror mounted on a piezo stage and a second arm containing the near-field probe and sample. Due to the relatively large size of the focused IR beam (about  $80\ \mu\text{m}$  in diameter, see inset Fig. 1) an illumination of the tip shaft and sample cannot be completely avoided, leading to a strong background contribution. For separating the intensive far-field signal from the relatively weak near-field contribution the interference signal is demodulated at the 2nd, 3rd, and 4th harmonics of the cantilever's oscillation frequency  $\Omega$ . This provides a signal with strongly decreasing background contribution for higher harmonics ( $n > 1$ ).

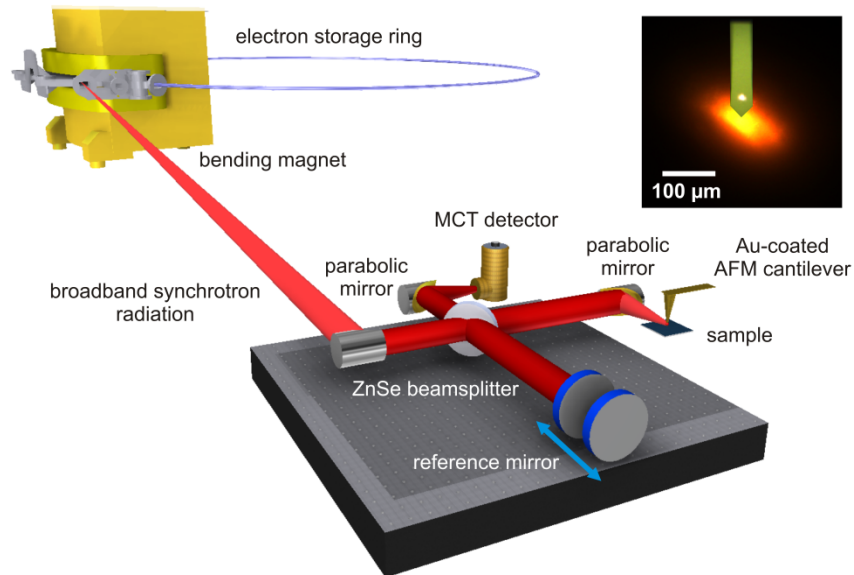


Fig. 1. Schematic diagram of the experimental s-SNOM setup using broadband synchrotron radiation in the IR regime from the electron storage ring MLS. The IR radiation is coupled out at a bending magnet and guided by several mirrors (not shown in the image) to the experimental setup. The focused IR beam has a diameter of about  $80\ \mu\text{m}$  (inset with an optical microscopy image).

For the acquisition of the interferogram the mirror in the reference arm of the interferometer is translated over a distance of up to  $800\ \mu\text{m}$ . The Fourier transformation of the obtained interferogram as a function of the optical beam path provides the corresponding nano-FTIR spectrum. The signal is detected by a liquid nitrogen cooled Mercury-Cadmium-Telluride (MCT) detector (Teledyne Judson Technologies, United States) with a sensitivity range from about  $2\ \mu\text{m}$  to  $13.5\ \mu\text{m}$ .

The near-field imaging experiments were performed on a sample with rectangular  $\text{SiO}_2$  patterns on a Si substrate. The  $\text{SiO}_2$  patterns had an edge length of  $1.5\ \mu\text{m} \times 1.0\ \mu\text{m}$  and a height of about  $20\ \text{nm}$ . The nano-FTIR spectra were recorded from a 6H-SiC bulk sample and different thin layers deposited on crystalline Si substrate such as  $10\ \text{nm}$   $\text{TiO}_2$  (anatase),  $30\ \text{nm}$   $\text{SiO}_2$  and  $50\ \text{nm}$  low-stressed non-stoichiometric  $\text{Si}_x\text{N}_y$ .

### 3. Results and discussion

Since near-field microscopy is typically performed with monochromatic light sources, we first validate nanoscale focusing of ultra-broadband IR synchrotron radiation by performing high-resolution near-field imaging on a semiconductor sample. For this purpose, the mirror in the

reference arm of the Michelson interferometer is placed at the white light position where the simultaneous interference of all spectral components leads to a maximum detector signal. In Fig. 2(a) a topography image and the simultaneously acquired optical image (2nd harmonic optical signal, in the following denoted as O2-signal) from the semiconductor sample are shown. The image has a size of 180 x 180 pixels with an integration time of 39 ms per pixel yielding a total acquisition time of about 20 minutes.

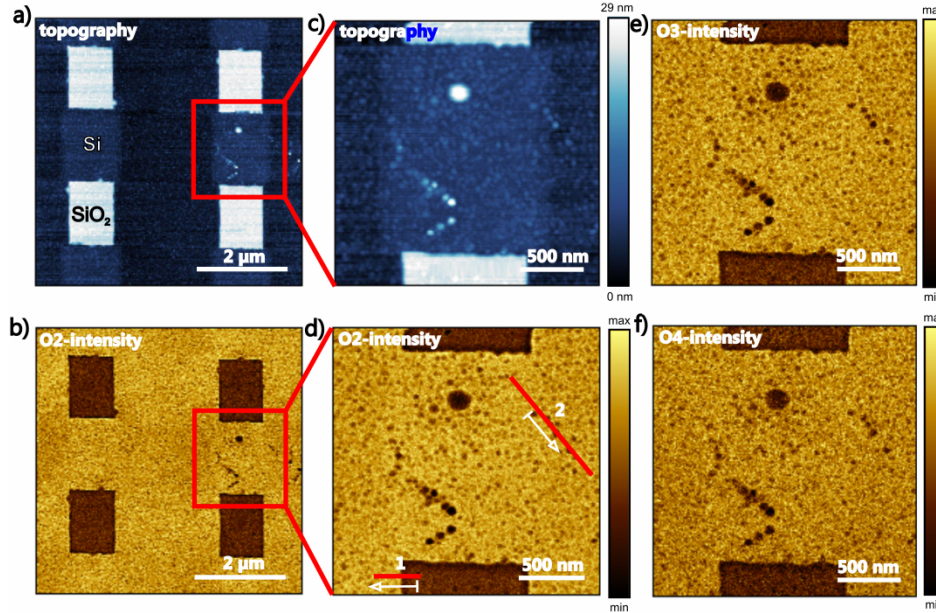


Fig. 2. Topography ((a) and (c)) and corresponding optical images (O2-, O3- and O4-signal) ((b), (d), (e), and (f)) obtained from a Si-sample with rectangular SiO<sub>2</sub> structures. The 20 nm high SiO<sub>2</sub> patterns with an edge length of 1 μm x 1.5 μm on (100) Si substrate appear bright in the AFM image and dark in the corresponding near-field image due to the stronger absorption of SiO<sub>2</sub> compared to Si in the mid-IR range. The acquisition time for the scan is about 20 minutes. The averaged current in the storage ring during the measurements was about 100 mA and the oscillation amplitude of the tip was set to about 50 nm. The red lines in (d) mark the position of the two scans (trace 1 and 2) shown in Figs. 3(a) and 3(b) while the scanning direction is indicated by the white arrows.

The four SiO<sub>2</sub> structures appear as bright rectangles on the Si substrate in the topography image. In the simultaneously recorded optical near-field image (Fig. 2(b)), the SiO<sub>2</sub> structures appear optically dark. This contrast in the near-field image can be explained by the average refractive index within the wavelength range of the incident IR radiation, which is lower for SiO<sub>2</sub> compared to Si substrate [38]. The results confirm that it is possible to obtain an optical image from the surface of a 6 μm x 6 μm large area of a semiconductor sample within a reasonable time and an acceptable signal-to-noise ratio up to the 4th harmonic (data not shown) by using synchrotron radiation.

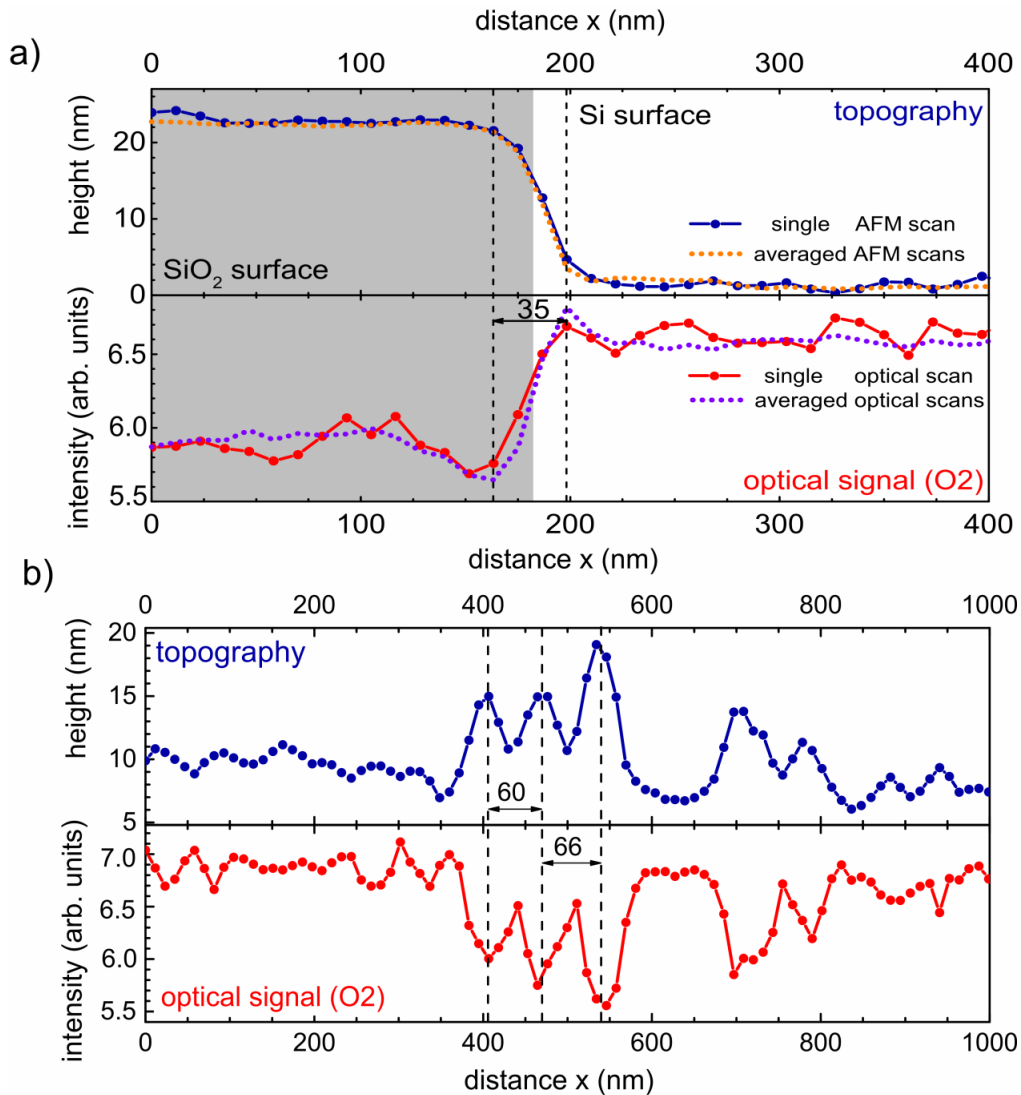


Fig. 3. Line scans performed across a SiO<sub>2</sub>-pattern edge and some nanoscale particles on the flat Si surface. The first line scan (a) is performed across the edge of a rectangular SiO<sub>2</sub> structure (see Fig. 2(d), trace 1). The AFM- and optical signal (O<sub>2</sub>-signal) change at the pattern edge (SiO<sub>2</sub> surface indicated by gray area) within a distance of < 40 nm. The averaged data obtained from 16 adjacent line scans across the same pattern edge are indicated by the dotted lines in the corresponding AFM and optical scan. The second line scan (b) illustrates the data obtained from three 5 nm to 10 nm height particles distributed over the plane Si surface (see Fig. 2(d), trace 2). According to the AFM and optical signals the distance between two adjacent particles is 60 nm and 66 nm.

For demonstrating that a spatial resolution significantly below the diffraction limit can be achieved, we scanned a smaller area (2 μm x 2 μm) as indicated by the red squares within the topography and 2nd harmonic optical image (O<sub>2</sub>-signal). The obtained AFM and corresponding optical images (O<sub>2</sub>-, O<sub>3</sub>- and O<sub>4</sub>-signal) are presented in Figs. 2(c)–2(f). In the topography and the optical images not only the oxide patterns but also several small contaminations spread over the Si surface are discerned, which can be used for a more accurate estimation of the attainable spatial resolution.

For this purpose the AFM and O<sub>2</sub>-optical data are presented in the two line scans illustrated in Figs. 3(a) and 3(b). The exact position of the two line scans is indicated in the O<sub>2</sub>-image (Fig. 2(d)) by the two red lines. The first line scan (trace 1) in Fig. 3(a) contains the data obtained from a scan performed across a SiO<sub>2</sub>/Si edge. According to the optical data the O<sub>2</sub>-signal intensity increases during the scan over the SiO<sub>2</sub>/Si edge within less than 40 nm. The simultaneously acquired AFM signal changes also within a comparable small distance. The second line scan (trace 2) in Fig. 3(b) (position indicated by the red line in Fig. 2(d)) presents the data from a scan across three particle-like structures located close to each other. According to the topography data the particles have a height of less than 10 nm and are separated by 60 nm and 66 nm, respectively. Despite their small size the O<sub>2</sub>-signal shows clear differences at the position of these three particles, demonstrating the high sensitivity of this imaging method. The achieved spatial resolution derived from the topography and the optical data is comparable, and hence, not determined by the wavelength of the incident radiation. Therefore, these results can be regarded as an experimental verification for the wavelength independency in near-field imaging using a scattering-type SNOM and a broadband radiation source that provides a much lower spectral energy density than SNOM experiments performed at a single wavelength with laser sources. Despite the use of the ultra-broadband IR synchrotron radiation the achievable spatial resolution is mainly determined by the diameter of the tip apex.

The main advantage of using broadband IR radiation, as used in the present study, is that it opens up the possibility to perform nano-FTIR spectroscopy over a wide frequency range. This enables the acquisition of near-field IR spectra from various thin surface layers or nanoscale structures. In order to demonstrate the high sensitivity and material discrimination capability of this technique, nano-FTIR spectra were collected from different samples, i.e. bulk materials (6H-SiC) and thin films (10 nm TiO<sub>2</sub> (anatase), 30 nm SiO<sub>2</sub>, and 50 nm Si<sub>x</sub>N<sub>y</sub>). For acquiring a FTIR spectrum the mirror in the reference arm of the Michelson interferometer can be moved over a distance of up to 800 μm. The light scattered from tip and sample is recorded together with the reference beam by a detector yielding, an interferogram as function of the optical beam path difference. The accessible frequency range is mainly determined by the sensitivity range of the MCT detector used for the measurements, limiting the spectroscopic information in the present case to the wavelength range from about 2 μm (5000 cm<sup>-1</sup>) to 13.5 μm (740 cm<sup>-1</sup>). Each recorded interferogram consists of 4096 data points. The acquisition time per data point for the investigated samples was between 32 ms (bulk SiC) and 203 ms (10 nm TiO<sub>2</sub>-layer). The interferograms collected from four different sample systems as a function of the optical path difference are presented in Fig. 4(a).

The nano-FTIR spectra (2nd harmonic spectra, in the following denoted as S2 spectra) obtained from subsequent Fourier transformation of the corresponding interferograms are displayed in Fig. 4(b). In far-field spectra of SiC a broad band appears between 790 cm<sup>-1</sup> and 950 cm<sup>-1</sup> [46]. The approach of the metal coated tip to the bulk SiC surface results in a strong enhancement and narrowing of the phonon induced spectral response [46] at about 920 cm<sup>-1</sup> [47] as shown in Fig. 4(b). The appearance of the longitudinal optical phonon mode at this frequency also confirms near-field signal detection. The other near-field IR spectra were acquired from thin surface layers consisting of SiO<sub>2</sub>, TiO<sub>2</sub>, and Si<sub>x</sub>N<sub>y</sub>, respectively. SiO<sub>2</sub> has also a strong near-field phonon resonance as indicated by the relatively long interference pattern in Fig. 4(a). The Fourier transformation reveals a peak at about 1132 cm<sup>-1</sup> (Fig. 4(b)) in the corresponding near-field spectrum which is attributed to the SiO<sub>2</sub> surface phonon polariton mode [27, 37, 48, 49]. Additionally, a wide shoulder appears at the low-frequency side and a second relatively small shoulder on the high-frequency side as also observed in recent s-SNOM studies [48, 50]. Compared to the far-field spectral response of SiO<sub>2</sub> the near-field phonon resonance is much sharper [47], as also observed for SiC.



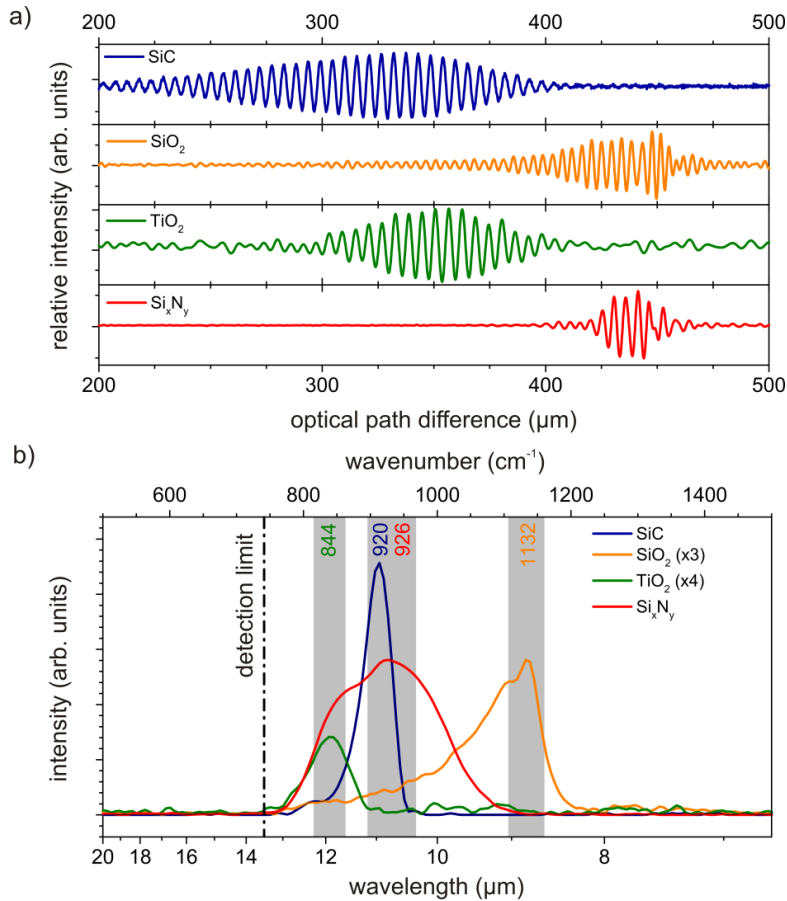


Fig. 4. Interferograms recorded from SiC, SiO<sub>2</sub>, TiO<sub>2</sub> (anatase) and Si<sub>3</sub>N<sub>4</sub>. The corresponding nano-FTIR spectra obtained from a subsequent Fourier transformation. The interferograms (Fig. 4(a)) were acquired from different samples with various layer thickness: bulk 6H-SiC, 10 nm TiO<sub>2</sub> (anatase), and 30 nm thick SiO<sub>2</sub>, and 50 nm Si<sub>3</sub>N<sub>4</sub>. The interferograms show the section from 200 μm to 500 μm of the optical beam path difference and were gathered by averaging four interferograms acquired successively at the same position. The nano-FTIR spectra (S2 spectra) from SiC, SiO<sub>2</sub>, TiO<sub>2</sub> (anatase), and Si<sub>3</sub>N<sub>4</sub> in (b) demonstrate the material discrimination capabilities of this method. (The near-field spectra of SiO<sub>2</sub> and TiO<sub>2</sub> were rescaled for better comparison. The numbers in the color of the corresponding curves and the gray bars indicate the position of the highest intensity.).

In the spectrum acquired from the 10 nm thin TiO<sub>2</sub> anatase layer the phonon resonance arises at about 844 cm<sup>-1</sup>. This corresponds to the longitudinal optical phonon mode that appears in far-field IR spectra in the wavenumber range between 835 cm<sup>-1</sup> to 875 cm<sup>-1</sup> [51]. With conventional far-field methods at perpendicular incidence this mode is typically very weak in the IR spectrum since the electric field has no significant component perpendicular to the surface of the TiO<sub>2</sub> layer [51]. In contrast, for grazing incidence the electric field has a much larger nonzero component perpendicular to the surface, enabling a more efficient excitation of longitudinal optical phonons. According to the dipole model [3] the electric field distribution between tip and sample can be described by a vertically oriented point dipole. Therefore, the strongest field between tip and sample is also vertically oriented allowing an efficient excitation of the longitudinal optical phonon modes, which explains the experimental results.

The near-field spectrum recorded from a 50 nm thick, low stressed, non-stoichiometric  $\text{Si}_x\text{N}_y$  layer deposited on Si substrate shows a relatively broad absorption peak between  $810\text{ cm}^{-1}$  and  $1100\text{ cm}^{-1}$  with a maximum at around  $926\text{ cm}^{-1}$ . Upon deconvolution the broad peak can be fitted by three symmetric Gaussian bands at  $849\text{ cm}^{-1}$ ,  $912\text{ cm}^{-1}$ , and  $961\text{ cm}^{-1}$ , which represent absorption states of the Si-N stretching mode [52–54]. Small band shifts in IR and Raman spectra can also be explained by the influence of stress as has been reported for SiC [34, 47] and other Si-based [55, 56] sample systems.

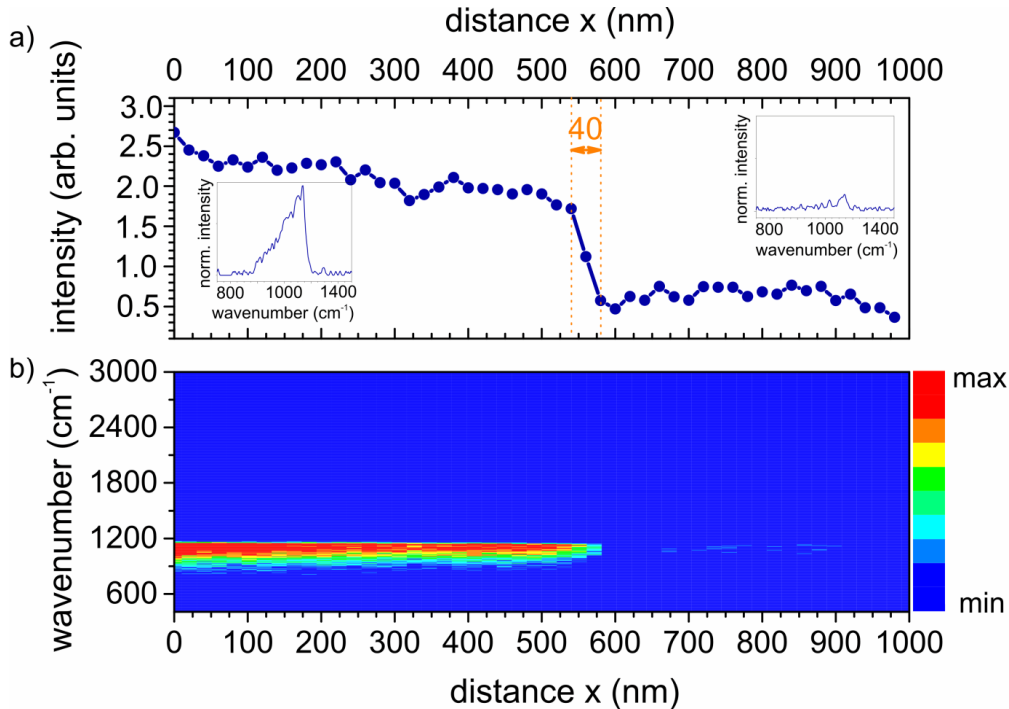


Fig. 5. Intensity (a) and spectroscopic nanoimaging (b) using ultra-broadband IR radiation provided by the electron storage ring MLS. The intensity (S2 spectra) from the Si phonon band at  $1135\text{ cm}^{-1}$  decreases within about 40 nm when performing a scan across a  $\text{SiO}_2/\text{Si}$  edge (cf. Fig. 2(d), trace 1) as documented in the two insets in Fig. 5(a) showing the two nano-FTIR spectra from the line scan recorded from the  $\text{SiO}_2$  and the Si surface. The same spatial resolution is obtained from spectroscopic nanoimaging as derived from results shown in Fig. 3(a). The spectral resolution is about  $6.25\text{ cm}^{-1}$ .

In order to demonstrate nano-FTIR mapping and the achievable lateral resolution in nanoimaging using synchrotron radiation a scan was performed across a  $\text{SiO}_2/\text{Si}$  edge as illustrated in Fig. 2(d) while recording 50 near-field IR spectra over a distance of 1000 nm. The obtained results are presented in Fig. 5. The intensity change during the scan within the wavenumber interval between  $962\text{ cm}^{-1}$  and  $1165\text{ cm}^{-1}$  is documented in Fig. 5(a). At the  $\text{SiO}_2/\text{Si}$  edge the intensity of the  $\text{SiO}_2$  phonon peak at about  $1135\text{ cm}^{-1}$  decreases to the noise level within a distance of about 40 nm. This is also illustrated in Fig. 5(b) showing the spectral change during the line scan. The intensive  $\text{SiO}_2$  phonon peak indicated by the red color (Fig. 5(b)) vanishes around the edge. In the Si area a very weak peak is still visible in the near-field spectrum (inset right side in Fig. 5(a)) which indicates a thin remnant  $\text{SiO}_2$ -layer in this region. According to reference [50] a trace of the  $\text{SiO}_2$  phonon resonance can be observed also for layers as thin as 2 nm. Due to the relatively low signal-to-noise ratio in the spectra recorded during the line scan, the increase of the secondary peak on the high-frequency side of the  $\text{SiO}_2$  peak was not observable.

The presented results clearly demonstrate that local material composition and properties can be probed with a spatial resolution at the nanoscale using broadband IR synchrotron radiation. The comparison of the results obtained from near-field imaging and spectroscopic nanoimaging show that a spatial resolution around 40 nm can be achieved.

#### **4. Conclusion**

In summary, we demonstrated synchrotron radiation-based near-field imaging of semiconductor structures with a lateral resolution of about 40 nm. The achieved optical resolution using ultra-broadband infrared radiation is comparable to the AFM resolution in topographic imaging, demonstrating the wavelength independence in near-field imaging. The main advantage of using broadband radiation source is the capability to acquire near-field IR spectra over a wide frequency range which is only limited by the sensitivity range of the detector and absorption of the optical components. The high sensitivity of nano-FTIR spectroscopy is shown to enable the spectroscopic characterization of thin films used in semiconductor technology.

#### **Acknowledgments**

The authors thank the MLS team and associates from PTB's X-ray and IR-Spectrometry group for helpful support and fruitful discussions. Some of the authors (P.H., C.F., A.He., A.Ho. and B.B.) acknowledge financial support by the European Metrology Research Programme (EMRP). This work was funded through the EMRP Projects IND54 Nanostrain, IND56 Q-AIMDS, and NEW01 TReND. The EMRP is jointly funded by the EMRP participating countries within EURAMET and the European Union. Financial support by the SFB 1112 is also gratefully acknowledged.